Dalton Transactions

PAPER

Cite this: *Dalton Trans.*, 2019, **48**, 14748

Controllable electrodeposition of binary metal films from deep eutectic solvent as an efficient and durable catalyst for the oxygen evolution reaction†

Truong-Giang Vo, Sebastian Dario Suarez Hidalgo and Chia-Ying Chiang *

Received 24th July 2019,
Accepted 10th September 2019

DOI: 10.1039/c9dt03028j

rsc.li/dalton

In this work, we present an easy and scalable electrodeposition protocol that operates in a deep eutectic solvent, used to prepare self-supported Ni–Fe alloy films directly grown on copper foils. Unlike electrodeposition in aqueous baths, alloy compositions deposited in deep eutectic solvent are found to be the same as in plating solution owing to the enlargement of the deposition window and secondary reaction suppression. By rationally tuning the Ni/Fe ratio in deep eutectic solvent plating solution, the best oxygen evolution reaction performance was achieved by a $Ni_{75}Fe_{25}$ catalyst, which requires only a 316 mV overpotential to reach a current density of 10 mA cm^{-2}, while its Tafel slope is as low as 62 mV dec^{-1}. This catalyst can operate at 10 mA cm^{-2} with negligible activity degradation for over 10 h, promising its potential use as a low-cost, high-performance and stable electrocatalyst in water splitting devices.

1. Introduction

Ni–Fe alloys are important materials that have attracted much attention for energy storage/conversion applications such as rechargeable metal–air batteries[1–3] and electrochemical water-splitting.[4,5] The electrodeposition of Ni–Fe alloys from aqueous baths is widely utilized as the most feasible method for low-cost mass production, owing to its high metal growth rate, low cost, and great flexibility, compared with other deposition techniques such as evaporation and sputtering.[6,7] The most common solvent for the electrodeposition of metal is water, but electrodeposition in aqueous electrolyte does not always work successfully because water itself is the cause of difficulties encountered during electrodeposition.[8] The narrow electrochemical window is the most common limit. In some cases, the reduction potential of the metal is so negative that it coincides with the limit of the electrochemical window on the cathode side. Then, metal cation reduction occurs in parallel to the solvent reduction (hydrogen evolution), leading to a loss in the electrochemical efficiency, low-quality deposition and even hydrogen embrittlement.[8,9] These inconveniences lead to a need for additives (such as fluoroboric acid,[10] glycolic acid,[11] citric acid,[12] D-manitol,[13] and ethylenediamine[14]), which can have negative effects on the electrodeposits due to the accumulation of the reduction products of the complexing agents during electrodeposition.[6,15] More importantly, the simultaneous electrodeposition of iron and nickel results in the phenomenon of anomalous co-deposition, *i.e.*, the reduction of nickel is inhibited under certain conditions while the deposition of the less noble metal is increased when compared to its individual deposition rate in a single metal plating bath.[16,17] Therefore, the composition of the electrodeposit often bears no resemblance to the electrolyte composition in which it is plated. In addition, the limited solubility of some metal ions in aqueous solution and water volatility also limits the choice of water as the solvent.

Alternatively, in the past decade, sustained efforts have been made to overcome the limitation of the electrodeposition process in aqueous solution. This has led to the development of deep eutectic solvents (DES), which are a class of ionic liquids consisting of a eutectic mixture of quaternary ammonium salts and a hydrogen bond donor species.[18] DES distinguish themselves from conventional water-based electrolytes in many ways such as (i) they are known as "green solvents" that have low toxicity and low vapor pressure that do not readily evaporate and can be used over a wide temperature range.[19,20] For instance, ethylene glycol, due to its high boiling point (197.6 °C), allows electrodeposition to take place at a higher temperature than water;[21] (ii) DES have much wider electrochemical windows than aqueous electrolyte, allowing the deposition of metals with very negative redox potentials;[22] (iii) DES can be aprotic, and thus problems with regards to hydrogen evol-

Department of Chemical Engineering, National Taiwan University of Science and Technology, Taipei-106, Taiwan. E-mail: cychiang@mail.ntust.edu.tw; Fax: +886-2-2737-6644; Tel: +886-2-2737-6641

†Electronic supplementary information (ESI) available. See DOI: 10.1039/c9dt03028j

ution, which are not usually avoidable in aqueous baths, can be solved.[15] These merits have led to the expectation that ionic liquids could be used effectively for the electrolytic deposition of alloys from binary metal ion mixtures that would not be possible in conventional aqueous electrolytes.

While significant progress has been made in scientific research on Ni and/or Fe-containing catalysts for the oxygen evolution reaction (OER) in recent years,[23–27] to the best of our knowledge, there are no published works that discuss controllable Ni–Fe electrodeposition involving DES systems for the OER. Moreover, it is well-known that the preparation method has significant effects on the catalyst performance. Therefore, the motivation of this study was to investigate the feasibility of using DES for metal electrodeposition and to evaluate its applicability as an electrocatalyst in water splitting.

2. Materials and methods

2.1. Electrocatalyst preparation

The DES was prepared by the mixing of choline chloride and ethylene glycol (Eg) in a molar ratio of 1 : 2 and stirring at 70 °C until a homogeneous liquid was obtained. Metal chloride salts ($NiCl_2{\cdot}6H_2O$ and/or $FeCl_3{\cdot}6H_2O$) were added to the prepared DES and stirred continuously at room temperature to ensure the dissolution process (details provided in Table S1, ESI†). Cu foil (0.1 mm, 99.99%) with an exposed area of 1 cm^2 was used as the substrate. Before each deposition process, a surface pretreatment sequence was conducted for the copper substrate. First, the copper substrate was polished using sandpaper (P2500, 3M) and then degreased using acetone. Afterwards, the removal of surface impurities was performed in 3% HCl solution. In order to determine the appropriate deposition potential, cyclic voltammetry (CV) was carried out in plating solution at a scan rate of 5 mV s^{-1} using a Pt disk as the working electrode. A carbon rod (3 mm in diameter) and Ag wire/ethaline were used as the counter and reference electrodes, respectively. The use of this kind of pseudo-reference electrode is attractive because the possible contamination from the working solution is avoided.[28] The potential of Ag remains constant due to the existence of the Ag/Ag^+ couple in such Cl^- ion enriched ionic liquids.[29,30]

The electrodeposition was carried out using an electrochemical workstation (Metrohm, Netherlands) under mild stirring at 60 °C and potentiostatic (potential control) conditions, as schematically illustrated in Scheme 1. For all of the deposition experiments, cathodic potentiostatic deposition was used, and −0.9 V was applied to pass a charge density of 3 C cm^{-2}, which took approximately 20 min. The concentration of Ni and Fe salts in the DES solution was also systematically tuned and a series of catalyst electrodes were obtained. Electrode samples with a molar ratio of Ni : Fe = 25 : 75 (total concentration of 0.2 M) in the deposition were labeled as $Ni_{25}Fe_{75}$, while other samples were named in the same format. After deposition, the catalyst film was rinsed with acetone and dried.

2.2. Materials characterization and electrochemical studies

Scanning electron microscopy (SEM) (JEOL JSM-6500F) at an accelerating voltage of 15 kV was carried out to examine the morphology of the electrodeposited samples. Both energy-dispersive X-ray spectroscopy (EDS) and inductively coupled plasma atomic emission spectrometry (ICP-AES, JY2000 Jobin Yvon) were performed to determine the chemical compositions of the Ni–Fe catalysts. Powder X-ray diffraction measurements were conducted using a D2 Bruker diffractometer at 30 kV voltage at increments of 0.1° per second. The chemical valences of the catalyst surfaces were studied by X-ray photoelectron spectroscopy (XPS) (VG Scientific ESCALAB 250). The recording of the UV-vis absorption spectra in the range of 200–800 nm was performed using a double-beam UV-Vis spectrophotometer (V670, Jasco). Two matched quartz cells of 1 cm optical path lengths were used, one for the sample solution and the other for the reference solution, *i.e.* the DES. Raman measurements were performed on a confocal Raman microscope system (MRID, Protrustech, Taiwan) with 532 laser as the excitation source.

The electrochemical performance of the catalysts towards the OER was evaluated in a standard three-electrode system connected to a potentiostat (Autolab, PGSTAT302N). As-prepared catalyst films, Pt mesh (2.5 cm × 2.5 cm) and Ag/AgCl (in 3 M KCl) were used as the working, counter and reference electrodes, respectively. CV measurements were carried out from 0.1 to 1.1 V *vs.* Ag/AgCl for 5 cycles at a scan rate of 10 mV s^{-1} before linear sweep voltammetry (LSV) measurements were carried out. Electrochemical impedance spectroscopy (EIS) was

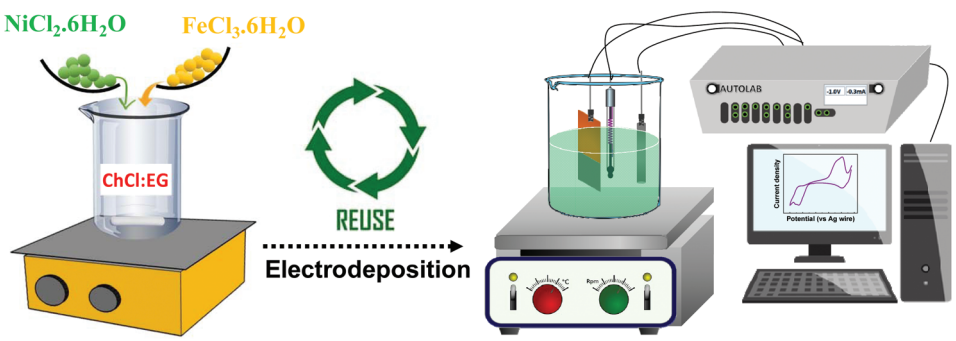

Scheme 1 Schematic illustration of the electrodeposition of Ni–Fe films in deep eutectic solvent.

conducted at an overpotential of 300 mV in the frequency range of 100 kHz to 0.1 Hz with a 10 mV sinusoidal amplitude. The polarization curves were corrected with ohmic drop compensation. All of the potentials in the OER study were converted to the reversible hydrogen electrode (RHE).

3. Results and discussion

At first, to obtain qualitative information on the possible species that exist in the electrolytes, UV-Vis spectra of the plating solution containing the single components and their mixtures in DES were recorded, as presented in Fig. 1. The spectrum for $NiCl_2{\cdot}6H_2O$ dissolved in DES presents three sets of absorption bands centered at 419, 690 and 765 nm, which corroborates a previously reported study.[31] The most intense absorption band at 419 nm can be attributed to the $^3A_{2g}(F) \rightarrow {}^3T_{1g}(P)$ transition of the octahedral Ni^{2+} ion.[32,33] The absorptions in the 690–765 nm region have recently been reported to be due to the presence of a $[Ni(Eg)_3]^{2+}$ complex.[34,35] The positions of absorption peaks in the 600–850 nm region remained invariable when the content of Ni^{2+} changed, whereas the absorbance became less pronounced with decreasing Ni content. It is also worth noting that there was also redshift of light absorption with an increase in the Fe content, which corresponds to a color change from pale green to orange (see the inset in Fig. 1).

Before doing the electrodeposition, knowing the electrochemical operating window of DES, which is an indicator of the evaluation of the stability of the plating solution, is important and is shown in Fig. S1.† As can be seen, the electrochemical window of pure DES is around −1.0 to 1.2 V *vs.* the Ag quasi-reference (hereinafter referred to as Ag). Within this potential range, no reaction was observed. Applying a more negative potential might cause the decomposition of both DES (reduction of Ch^+ in chlorine chloride)[36,37] and water present in the solution (due to the hygroscopic nature of DES). On the other hand, the anodic limit was observed at 1.0 V *vs.* Ag where the oxygen evolution reaction started at the working electrode. Afterwards, a series of cyclic voltammetry measurements in DES containing Ni and Fe salts were conducted from the open circuit potential (OCP) to −1.2 V *vs.* Ag. As shown in Fig. 2, the OCP shifted positively from −0.4 V *vs.* Ag for DES containing Ni salt only and increased gradually to −0.25 V *vs.* Ag for Fe salt only. The recorded voltammogram for Ni shows that the onset potential for reduction of Ni^{2+} to Ni^0 began at −0.65 V *vs.* Ag. A second reduction process occurred at around −1.0 V *vs.* Ag, either corresponding to the electrolysis of the coordinated water or breaking down of the electrolyte, as bubbles were observed at the cathode. In the anodic scan, no oxidation peak was observed, suggesting that the stripping of Ni requires a higher positive potential. On the other hand, the voltammogram for Fe shows two clear reduction waves. The first one appeared at −0.25 V *vs.* Ag, which is attributed to the reduction of Fe^{3+} to Fe^{2+} and the second one appeared at around −0.9 V *vs.* Ag where the reduction of metallic Fe occurred. At a potential more negative than −1.1 V *vs.* Ag, the generation of bubbles was noticed. During the anodic sweep, the wave appeared at around −0.5 V *vs.* Ag, representing the oxidation of Fe^0 to Fe^{2+} and consecutively Fe^{2+} to Fe^{3+}. While mixing Ni and Fe salts together in the DES plating solution, the recorded CV presented a negative shift in the onset potential for the reduction of Ni compared with that of Ni salts only. During the anodic sweep, the anodic current for the oxidation from Fe^0 to Fe^{2+} showed a positive shift with an increase in Ni salt in the DES plating solution compared with that of the plating solution containing Fe salt only. It should also be noted that the onset reduction potential in DES for Ni (−0.65 V *vs.* Ag) and for Fe (−0.9 V *vs.* Ag) were close to each other. This strongly indicates that Ni–Fe co-deposition can be easily achieved from DES without adding a complex agent,

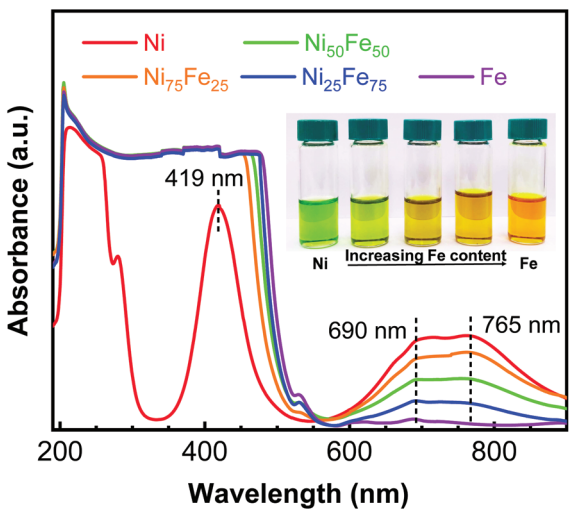

Fig. 1 UV-vis spectra measured at room temperature for liquid mixtures containing DES and Ni/Fe in various ratios.

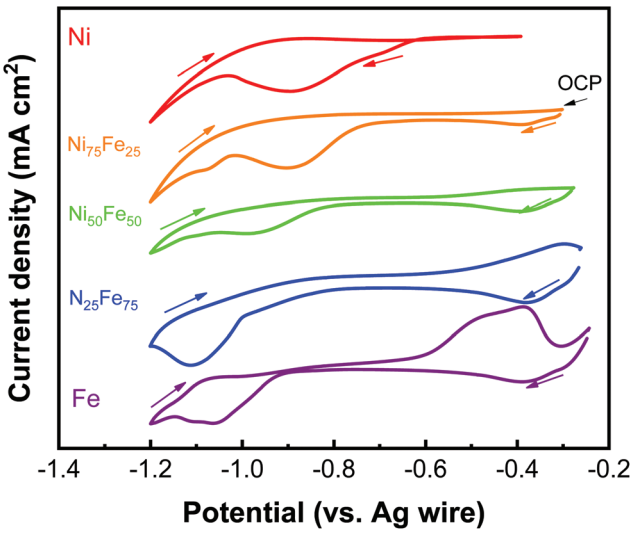

Fig. 2 Cyclic voltammetry of Ni, $Ni_{75}Fe_{25}$, $Ni_{50}Fe_{50}$, $Ni_{25}Fe_{75}$, and Fe in DES on Cu substrate, recorded from open circuit potential to −1.2 V *vs.* Ag at a 5 mV s^{-1} scan rate at 60 °C.

which is indispensable in an aqueous plating solution.[38] Based on these results, a potential of −0.9 V *vs.* Ag was selected for the electrodeposition of Ni–Fe alloys, which allows both metals to be deposited and prevents the breakdown of the DES and/or bubble formation.

Fig. 3 shows the SEM images of the electrodeposited films. It is clear that various morphologies for the Ni and Fe films were observed. The Ni film showed nodular grown deposits with a size of 100–200 nm, while the Fe film showed submicron scale particles. Furthermore, comparing the surface morphology of the three different composition Ni–Fe alloys, the films with a high Fe content showed a slightly more submicron scale particle-like structure, which might be due to the instantaneous nucleation of iron electrodeposition.[39,40] A typical cross-sectional image of a Ni–Fe film obtained on a Cu substrate in DES is shown in Fig. S2.† It is clear that the Ni–Fe layer deposited from DES was uniformly dense with a thickness of approximately 10–12 μm.

Table 1 summarizes the concentration of Ni and Fe in the DES plating solution and the actual content in the resultant films analyzed by EDS and ICP-AES. It is evident that the compositions of the Ni–Fe films were close to the metal–cation ratio in the plating solution, which is similar to in previously reported results.[41] It is further confirmation that the composition of a Ni–Fe alloy deposited in a DES solution was directly proportional to the metal concentration in the plating solution owing to the wider electrochemical window and absence of hydrogen evolution in the DES. Subsequently, the *in situ* formation/precipitation of iron hydroxide on the electrode surface and competitive adsorption[42–44] can be avoided and thus a non-anomalous co-deposition of Ni–Fe alloys was achieved.[16]

Table 1 Composition of the electrodeposited Ni–Fe films obtained from electrodeposition in DES determined by EDS and ICP-AES

	Film composition by EDS		Film composition by ICP-AES	
Ni/Fe ratio in DES	Ni (%)	Fe (%)	Ni (%)	Fe (%)
75 : 25	74 ± 1.9	26 ± 1.9	73 ± 0.6	27 ± 0.6
50 : 50	51 ± 2.1	49 ± 2.1	46 ± 2.2	54 ± 2.2
25 : 75	27 ± 1.4	73 ± 1.4	23 ± 0.4	77 ± 0.4

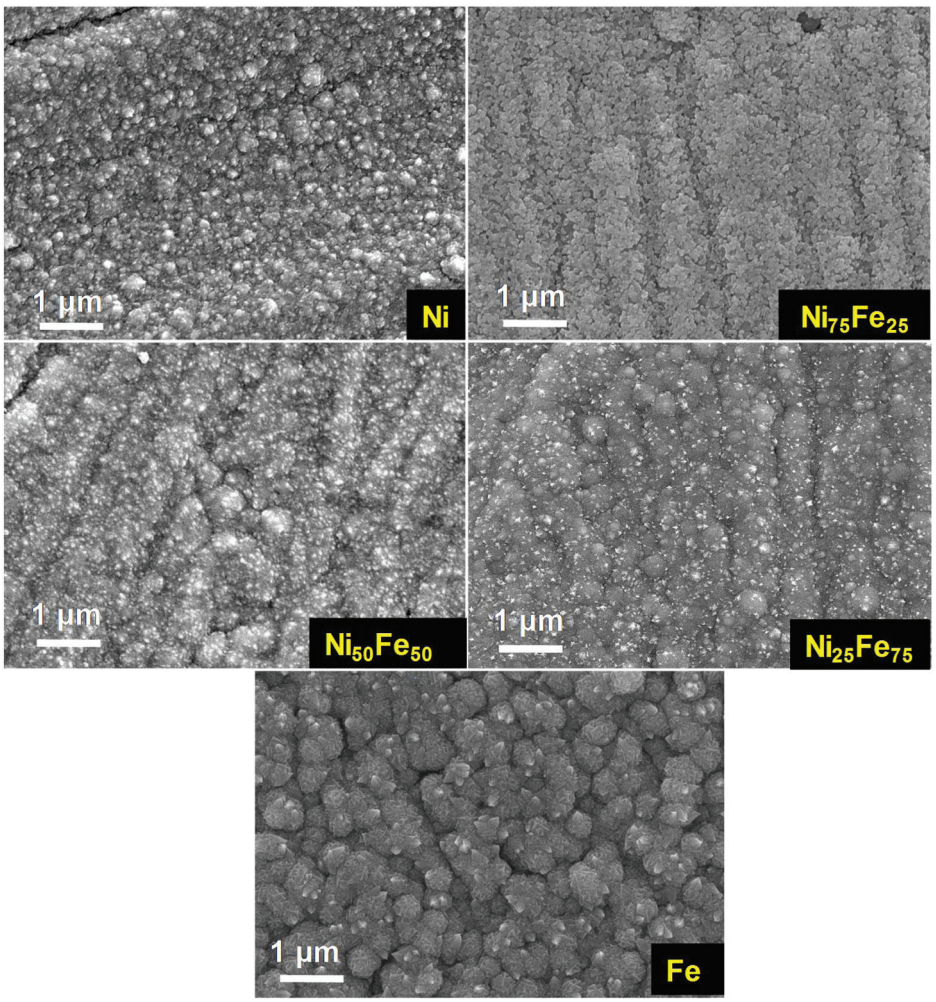

Fig. 3 SEM images of various Ni–Fe films electrodeposited in deep eutectic solvent.

X-ray diffraction (XRD) measurements were performed to investigate the crystal structures of the electrodeposited Ni–Fe films in various deposit compositions. Fig. 4 shows a series of XRD patterns of scratched powders from Ni, Fe and Ni–Fe alloy film samples electrodeposited from DES solutions. The Ni showed a diffraction pattern at (111), (200), and (220), which indexes to face-centered cubic (fcc) Ni metal. The Fe sample showed peaks for both body-centered cubic (bcc) metallic iron and iron oxide.[45] The XRD patterns of the Ni–Fe alloy samples showed characteristic diffraction peaks that match fcc Ni and a bulk NiFe alloy phase. Notably, the diffraction line at (111) shifted to higher 2θ angles as a consequence of decreased d-spacing when a higher percentage of iron was accommodated in the unit cell.[46] The variation in the d-spacings and lattice parameters (a) for the Ni–Fe films with different percentage of added iron were also calculated and are tabulated in Table S2.† The lattice parameters showed an increasing trend when more Fe was inserted into the lattice, owing to the larger atomic radius of Fe compared to that of Ni.[46] However, upon a further increase in the Fe content from 50% to 75% for $Ni_{25}Fe_{75}$, its lattice parameter slightly decreased from 3.585 to 3.521 Å, which can be attributed to the phase transformation from fcc to bcc. This typical phase transition was also observed by Dijith and co-workers when about 80% Fe was present in an alloy.[46] To gain further information on the structures of various Ni–Fe films, Raman spectroscopy was performed on each sample in order to verify the possible materials formed on the surface of the metals. Fig. 4(b) shows the composition-dependent Raman frequencies of the Ni–Fe films. For the Ni only sample, it was inferred that the peaks at around 385 to 560 cm^{-1} are due to the stretching vibrations of Ni–O,[47] which consist predominantly of NiO and a small amount of $Ni(OH)_2$ on the surface of pure nickel. The broad peak at 450–472 cm^{-1} indicates the bending vibration of $Ni(OH)_2$, while the peak at around 497 cm^{-1} originates from NiO.[47,48] Raman spectra of the Ni–Fe films show that the Ni–O environment was modified by Fe incorporation, in which broader peaks with higher degrees of disorder were observed.[5,24] Regarding the Fe only film, a broad peak can be attributed to the existence of Fe-based oxides, possibly Fe_2O_3 and/or Fe_3O_4. The above information suggests that the surface of metallic films might *in situ* transform into metal oxides or hydroxides when they were exposed to an environment containing O_2 and moisture.[49,50]

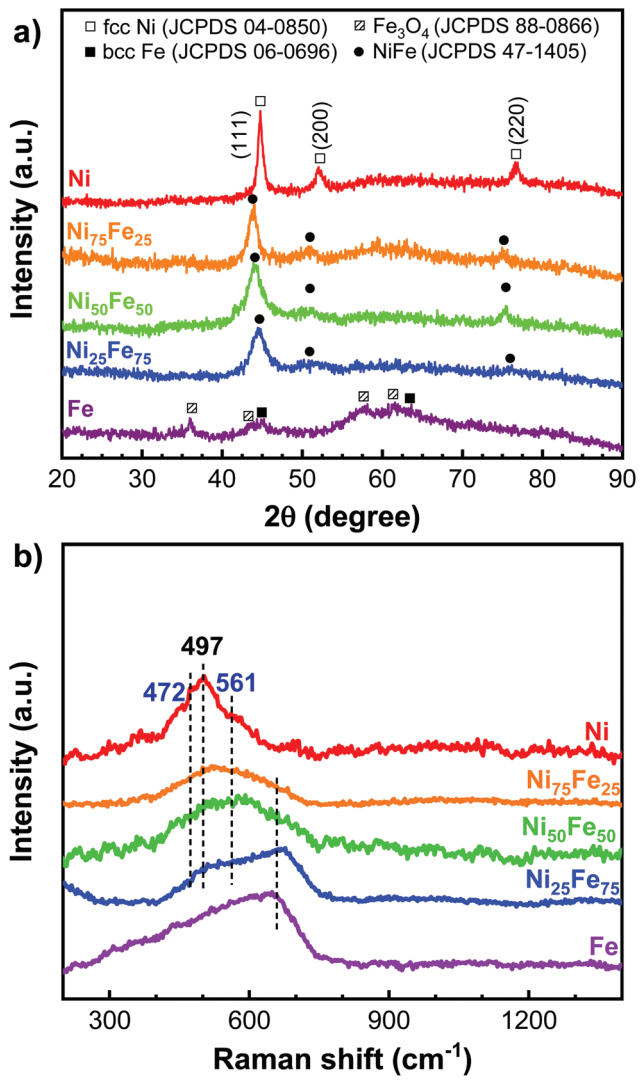

Fig. 4 Powder XRD patterns (a) and Raman spectra (b) of Ni, Fe and Ni–Fe samples obtained from electrodeposition in DES at T = 60 °C under a constant potential of −0.9 V *vs.* Ag.

XPS was further employed to gain more insight into the surface composition. Fig. 5 shows the XPS data of the Ni–Fe films, where the core level spectra of Ni and Fe 2p are presented. The peak centered at about 853.4 eV corresponds to metallic Ni in the alloy. The peaks centered at 855.7 and 858.6 eV can be attributed to Ni^{2+}/Ni^{3+} species. The peaks located at 710.1 and 712.5 eV in the Fe 2p spectra can be assigned to Fe^{3+}. Given that the surfaces of the Ni–Fe films may be easily oxidized in ambient air and that the surface compositions of these alloys may be unintentionally modified, the Ni–Fe film was therefore slightly sputtered to remove a few superficial monolayers by Ar^+ ion bombardment. The resulting chemical-state composition for the typical $Ni_{75}Fe_{25}$ film is shown in Fig. S3.† The appearance of metallic Fe^0 peaks at 706.6 eV together with an increase in Ni^0 (835.4 eV) after surface cleaning, suggests that only the top surface layer of the alloy was oxidized when it was exposed to the environment containing O_2 and moisture.[49,50]

After structural analysis, the Ni–Fe films prepared by electrodeposition in DES were assessed to determine whether or not they could be used as potential OER electrocatalysts. Five selected Ni_xFe_{100-x} (x = 0, 25, 50, 75 and 100) electrodes were used as the working electrode and LSV measurements were conducted in 0.1 M KOH. Continuous CV measurements were performed until a stable CV was observed before LSV measurements were conducted. The corresponding LSV curves are shown in Fig. 6. In 0.1 M KOH electrolyte, all of the samples exhibited significant differences in both the characteristic redox peaks and OER activity. The electrodeposited Ni sample displayed redox peaks at ~1.38 V during the anodic scans,

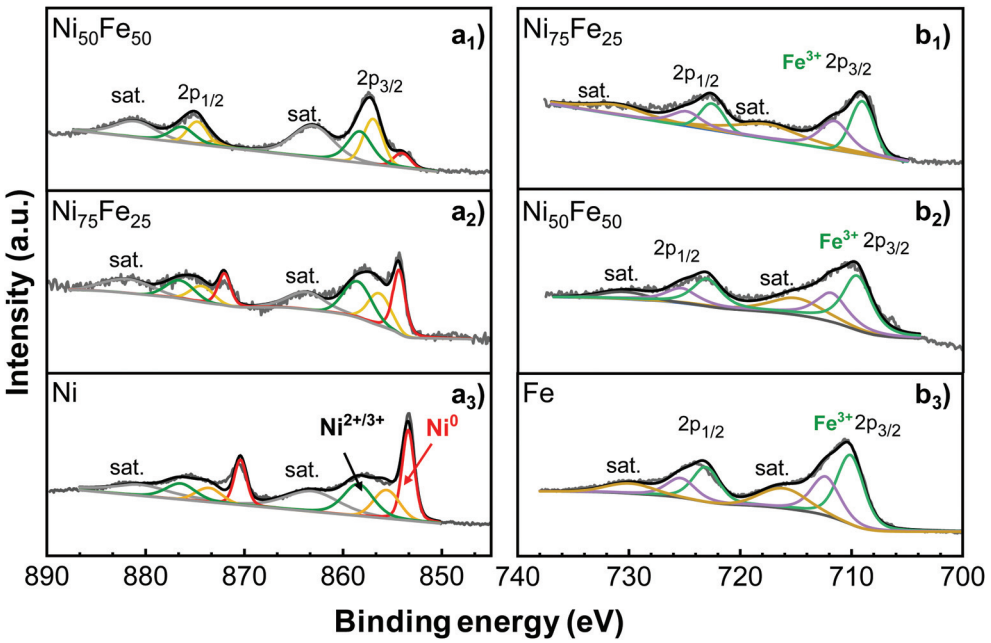

Fig. 5 Ni 2p (a_1–a_3) and Fe 2p (b_1–b_3) XPS spectra of mixed Ni–Fe films electrodeposited in DES of the various catalyst compositions.

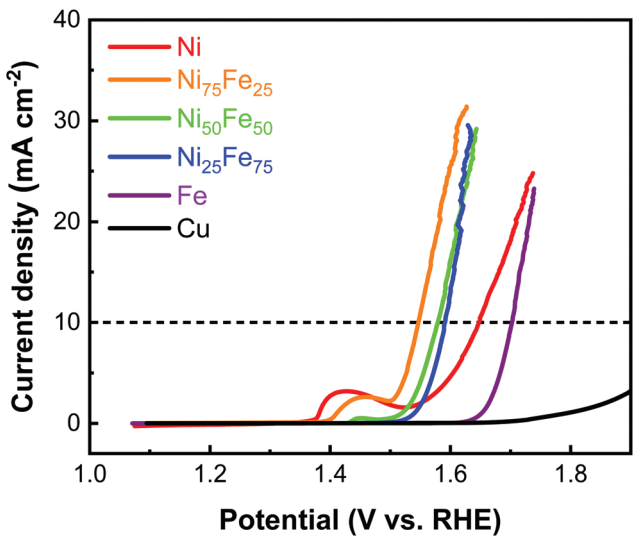

Fig. 6 Electrochemical characterization for the OER of mixed Ni–Fe films electrodeposited in DES with various catalyst compositions.

which can be attributed to the oxidation of Ni^{2+} to Ni^{3+} due to the formation of nickel hydroxide/oxyhydroxide on the metal surface in alkaline electrolyte.[51] Meanwhile, the Fe film showed no observable redox features and remained nominally Fe^{3+}, in line with a previous report.[24] For the Ni–Fe bimetallic catalysts, their corresponding voltammograms differ noticeably according to their $Ni(OH)_2$/NiOOH redox characteristics. As a higher amount of Fe was incorporated, the $Ni(OH)_2$/NiOOH oxidation peaks shifted positively to higher potentials and the redox peak areas decreased simultaneously.[24,52] At an Fe content of 50%, the surface interconversion peak became less pronounced and even overlapped with the rapidly increasing OER current. The positive shift in the surface interconversion peaks indicates a strong electronic interaction between Ni and Fe due to the electron pull effect of Fe and that the electrocatalytic activity of Ni has been modified by the co-deposition of Fe into the Ni deposit. There have been similar phenomena reported for Ni–Fe layered double hydroxides,[53] Ni–Fe oxides,[54] Co–Fe oxides[55] or Co–Fe oxyhydroxides.[56] However, the OER activity of the Ni–Fe catalysts was not monotonically enhanced with increasing Fe content. The $Ni_{75}Fe_{25}$ sample exhibited the highest OER activity among the films produced here, giving an OER current density of 10 mA cm^{-2} with an overpotential of 316 mV, compared to 417 mV for the monometallic Ni catalyst. The OER activity decreased when the Fe content was greater or equal to 50%. For instance, the OER overpotential on $Ni_{25}Fe_{75}$ at 10 mA cm^{-2} increased to 361 mV. This activity drop is likely due to the decrease in the number of Ni active sites on the catalyst surface with the addition of more Fe.[24,51,52,57] These results are supported by a recent literature study, which reported that for a Ni-rich composition, the optimal Fe content varies from 10% to 50%.[52] Moreover, a blank LSV test on Cu foil (without catalyst deposition) was performed under the same experimental conditions to investigate the effect of the Cu foil substrate on the OER activity. In the overpotential region of <470 mV, a very low current density was observed. Thus, Ni–Fe bimetallic contributes to the high OER performance achieved on the reported $Ni_{75}Fe_{25}$ catalysts rather than the Cu foil substrate.

Besides the overpotential at a fixed current density, the Tafel slope is generally considered as another key parameter by which to evaluate the properties of an OER catalyst.

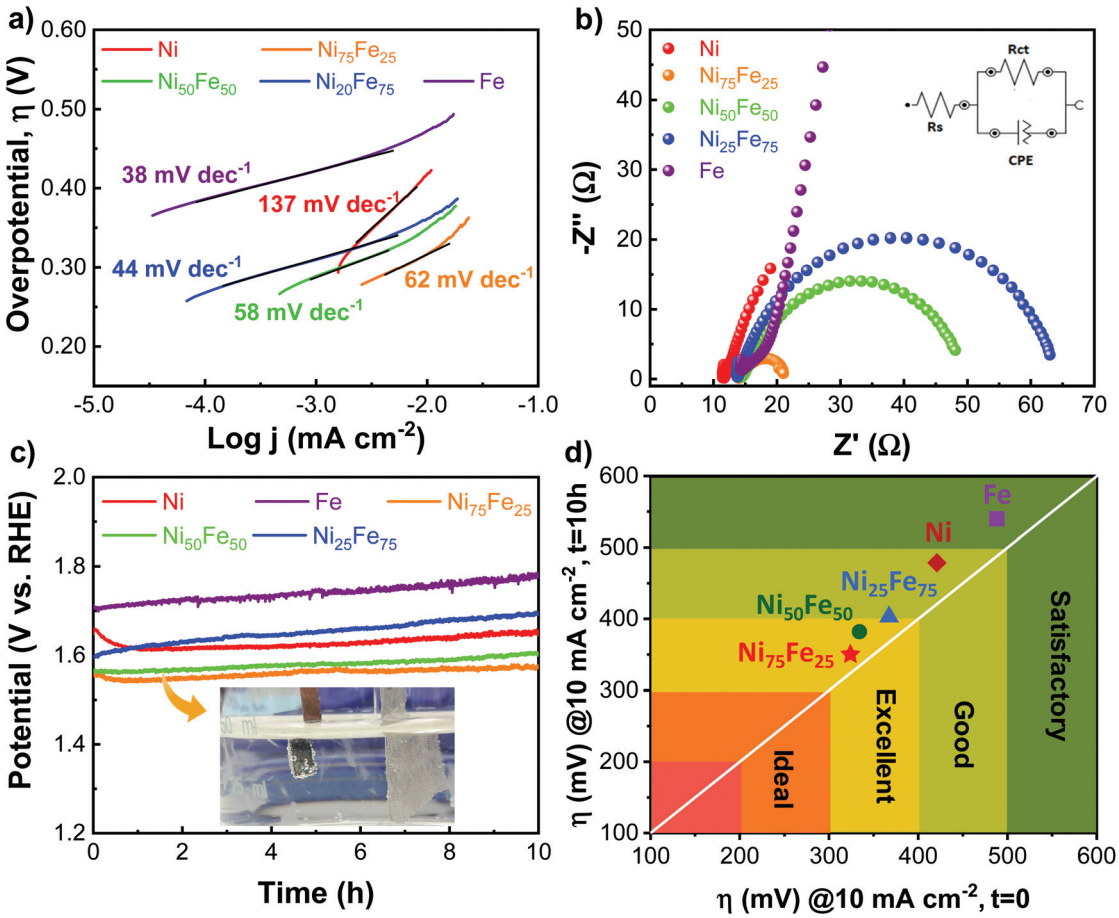

Fig. 7 (a) Tafel plots, (b) electrochemical impedance spectroscopy at an overpotential of 300 mV for OER, (c) chronopotentiometry at 10 mA cm^{-2} for 10 h and (d) the figures of merit for the OER.

Therefore, to gain further information into the OER kinetics, Tafel slopes derived from the corresponding polarization curves were constructed and are presented in Fig. 7(a). In practice, a smaller Tafel slope is preferred, which indicates a faster increase in the catalytic current with a smaller increment in the overpotential.[58] As shown in Fig. 7(a), the calculated Tafel slope for the Ni sample was 137 mV dec^{-1}, whereas the Fe deposit showed a Tafel slope at around 40 mV dec^{-1}, indicating that the Fe sample requires less of an overpotential to increase the OER rate by an order in magnitude than the Ni electrodeposited film. The Tafel slope value for the $Ni_{50}Fe_{50}$ alloy was 58 mV dec^{-1}, lower than the 62 and 137 mV dec^{-1} values observed for $Ni_{75}Fe_{25}$ and Ni, respectively. The smaller Tafel slope indicates that the incorporation of an appropriate amount of Fe into Ni-based materials can adjust the catalytic activity properties by tuning of the intrinsic kinetics.[59] However, it should be noted that Fe-rich films required a higher onset potential for the OER. To further understand the reasons underlying the excellent OER activity of the Ni–Fe films, we compared the electrochemical surface areas of the various electrodes, which were estimated from their double-layer capacitance (C_{dl}). As shown in Fig. S4,† despite the $Ni_{25}Fe_{75}$ and Fe samples displaying a nearly 4-fold increase in the surface area, they did not show the highest OER performance, indicating that the surface area difference caused by their different morphologies did not play a critical role in this study.

EIS measurements were conducted at an overpotential of 300 mV to study the charge transfer kinetics of the samples. The corresponding Nyquist plots were then obtained by fitting the impedance spectra with an equivalent Randles circuit model, showing the solution resistance (R_s), charge transfer resistance (R_{ct}), and a constant-phase element (CPE). These parameters are summarized in Table S3.† R_s was used for ohmic drop correction, R_{ct}, which is represented quantitatively by the diameter of the semicircle formed in the Nyquist plot, is related to the kinetics of the OER. The smaller the diameter, the faster the kinetics for the electron transfer process at the electrode and electrolyte interface. As shown in Fig. 7(b), there is no semicircle for pure Ni and Fe films, indicating that no obvious faradic process occurs at an applied overpotential of 300 mV during EIS analysis. This is in line with the LSV, where it can be noticed that the OER did not occur at the mentioned overpotential. The $Ni_{75}Fe_{25}$, $Ni_{50}Fe_{50}$, and $Ni_{25}Fe_{75}$ films each showed a semicircle, indicating that a faradic process occurs corresponding to the OER. The respective values of the charge

transfer resistance R_{ct} are 8, 37 and 51 Ω, respectively. This variation in the tendency of the R_{ct} values is consistent with the OER performance, where the current density is higher for $Ni_{75}Fe_{25}$ followed by $Ni_{50}Fe_{50}$ and $Ni_{25}Fe_{75}$ at a 300 mV overpotential. This clearly shows that the $Ni_{75}Fe_{25}$ sample had a more favorable environment for charge transfer. As a result, the OER was easier due to the reduced charge transfer barrier. The synergistic effect between Ni and Fe led to a decrease in R_{ct} and an acceleration in the charge transport.

The long-term stabilities of the samples obtained from electrodeposition in DES were also tested at a constant current density of 10 mA cm^{-2} (Fig. 7c) and their performances were evaluated based on a standardized protocol[60] (Fig. 7d). In the case of the monometallic Ni or Fe films, the potentials required to remain at 10 mA cm^{-2} increased by 90 mV over the course of 10 h, indicating satisfactory stability for the OER. The increase in the overpotential can also be attributed to the formation of oxides that are less conductive. A similar trend was found for $Ni_{25}Fe_{75}$. Interestingly, the $Ni_{75}Fe_{25}$ and $Ni_{50}Fe_{50}$ hybrid films showed excellent stability. Even after 10 h of continuous OER, the potential increased by only about 40 mV. On the other hand, it is believed that some of the total potential increase is due to oxygen bubbles blocking the electrode surface. The Ni–Fe hybrid electrodes are therefore highly active and stable OER electrocatalysts.

Table 2 presents a comparison of the kinetics parameters and catalyst performances for the nickel- and iron-containing materials reported so far. Interestingly, the Ni–Fe hybrid films electrodeposited from deep eutectic solvent exhibit competitive catalytic activity compared with many of the newly reported (Ni, Fe)-containing catalysts, especially when taking into account industrial scale-up issues,[57,64–66] highlighting their potential use as low-cost, high-performance and stable oxygen evolution catalysts in water splitting devices. For instance, Fominykh *et al.* have reported the synthesis of $Fe_xNi_{1-x}O$ nanoparticles at relatively high temperatures of 205 °C for 20–30 h using a solvothermal method.[57] Song and Hu presented the synthesis of a Ni–Fe-based catalyst using the hydrothermal method at 150 °C for two days followed by 24 h of exfoliation.[64] Zhang *et al.* reported a procedure to fabricate Ni–Fe hybrid electrocatalysts by pyrolysis of metal salts that requires a temperature of as high as 700 °C under inert atmosphere.[65] Such procedures usually require either special equipment, a high processing temperature or complicated and time-consuming synthesis procedures, thus creating scale-up difficulties.

It is noted that Ni/Fe-containing alloys very likely transform into their (oxy)hydroxides, which are generally recognized as an active water oxidation site for water splitting. XPS was therefore employed to gain further insights into the surface chemical composition of the nickel-rich alloys before and after running the OER for 10 h. Fig. S5 and S6† show the XPS data of the Ni–Fe alloys, where the core levels of Ni 2p and Fe 2p are presented. The doublet at 853.1/870.5 eV can be ascribed to Ni^0, representing the metallic Ni in the alloy. The peaks located at around 855.8 and 858.1 eV can be assigned to Ni^{2+} and Ni^{3+}, respectively, while an additional peak at 862.1 eV corresponds to a shake-up satellite characteristic of nickel oxide/hydroxide. Fig. S5† shows the reduction in the amount of metallic Ni and the increase in the quantity of higher valence species due to the oxidation of the metallic nickel after the OER. For the Fe element, although it is hard to accurately identify the iron phases present due to the similarities in their binding energies and spectral peaks, the presence of peaks located at around 710.8 and 714.9 eV and the absence of a metallic Fe characteristic peak (706.5 eV) indicates that iron is predominantly in the Fe^{3+} state after the OER (Fig. S6†). As shown in Fig. S7,† there were three peaks located at 529.8,

Table 2 Comparison of the electrocatalytic performance for various catalysts containing Ni and Fe

Catalyst/substrate	Synthesis method	Tafel slope (mV dec^{-1})	η (mV)	Stability test[a]	Reference
$Ni_{75}Fe_{25}$/Cu foil	Electrodeposition in DES	62	316	30 mV increment over 10 h	This study
$Ni_{50}Fe_{50}$/Cu foil		58	321	20 mV increment over 10 h	
$Ni_{25}Fe_{75}$/Cu foil		44	361	~90 mV increment over 10 h	
$Fe_{0.5}Ni_{0.5}O_x$	Solvothermal	72	584	—	61
NiFeO/GC	Coprecipitation	42	328	Stable over 12 h	62
NiFe/Au	Electrodeposition	58	330	—	63
$Fe_{0.9}Ni_{0.1}O$/Au	Solvothermal	37	297	~30 mV increment over 10 h	57
NiFe/NF	Electrodeposition	33	245	Stable over 10 h @25 mA cm^{-2}	23
NiFe LDH/NF	Hydrothermal	40	310	~25 mV increment over 10 h	64
NiFe/Au	Electrodeposition	42	330	—	24
$NiFe(OH)_2$/Ni foil	Electrodeposition	33	—	Stable over 10 days @1 A cm^{-2}	25
$Ni_{0.9}Fe_{0.1}$/GC	Pyrolysis	45	330	Stable over 24 h	65
$Ni_{50}Fe_{50}$/GC	Sonochemical	31	290	Stable over 12 h	66
NiFe/GC	Coprecipitation	41	320	76% over 10 h	67
Ni_2Fe/rGO	Hydrothermal	—	285	40 mV increment over 10 h	50
$FeNi_{4.34}$@FeNi-foil	Calcination	53	283	1000 potential cycle	27
$NiFe/CN_x$	Calcination	59	360	—	68
NiFeOH/NF	Impregnation	55	342	10 mV increment over 10 h	26

[a] At a constant current density of 10 mA cm^{-2} unless otherwise stated; η: overpotential required for 10 mA cm^{-2}; NF: nickel foam; GC: graphitic carbon; LDH: layered double hydroxide.

531.7 and 532.8 eV, which can be assigned to lattice oxygen, substituted hydroxyl groups and surface physi-/chemisorbed H_2O, respectively. The relative ratios of the OH^-/O^{2-} peaks increased after OER, proving the formation of (oxy)hydroxides on the surfaces of the films.

4. Conclusions

In summary, self-supported Ni–Fe hybrid films grown on Cu foils were successfully fabricated *via* a facile potentiostatic electrodeposition route in deep eutectic solvent. Owing to the wide operating window and compression of the redox potential in deep eutectic solvent, the deposited Ni–Fe films have the same composition as the plating solution. By tuning the Ni/Fe ion ratio in the DES plating solution, the $Ni_{75}Fe_{25}$ hybrid film shows the best OER performance, reaching 10 mA cm^{-2} at a low overpotential of 316 mV and maintaining its durability for 10 h. We believe that this facile one-step and scalable fabrication process in DES can be extended to fabricate other transitional metal-based materials for energy conversion and storage applications.

Conflicts of interest

There are no conflicts to declare.

Acknowledgements

This work was financially supported by the Young Scholar Fellowship Program by the Ministry of Science and Technology (MOST) in Taiwan, under Grant MOST108-2636-E-011-001. The authors would like to express their gratitude to the National Taiwan University of Science and Technology for facilities support.

References

1 D. Kubo, K. Tadanaga, A. Hayashi and M. Tatsumisago, *J. Mater. Chem. A*, 2013, **1**, 6804–6809.
2 W. Qiu, H. Xiao, W. He, Y. Li and Y. Tong, *Inorg. Chem. Front.*, 2018, **5**, 1805–1815.
3 P. Li, Z. Jin and D. Xiao, *J. Mater. Chem. A*, 2017, **5**, 3274–3283.
4 P. Du and R. Eisenberg, *Energy Environ. Sci.*, 2012, **5**, 6012–6021.
5 M. Gong and H. J. Dai, *Nano Res.*, 2015, **8**, 23–39.
6 S. Fazli and M. E. Bahrololoom, *Trans. IMF*, 2016, **94**, 92–98.
7 C. Su, F. He, H. Ju, Y. Zhang and E. Wang, *Electrochim. Acta*, 2009, **54**, 6257–6263.
8 P. De Vreese, PhD. Thesis, Katholieke Universiteit, Leuven, 2013.
9 J. Gong, S. Wang, X. Guo, L. Peng, H. Yang, R. Zhu, W. Ding and J. Dai, *Appl. Surf. Sci.*, 2013, **288**, 530–536.
10 C. Su, F. He, H. Ju, Y. Zhang and E. Wang, *Electrochim. Acta*, 2009, **54**, 6257–6263.
11 A. Afshar, A. G. Dolati and M. Ghorbani, *Mater. Chem. Phys.*, 2003, **77**, 352–358.
12 V. C. Kieling, *Surf. Coat. Technol.*, 1997, **96**, 135–139.
13 M. Lieder and S. Biallozor, *Surf. Technol.*, 1985, **26**, 23–34.
14 T. M. Harris, J. L. St. C. Wilson and M. Bleakley, *J. Electrochem. Soc.*, 1999, **146**, 1461–1464.
15 N.-C. Lo, P.-C. Chung, W.-J. Chuang, S. C. N. Hsu, I.-W. Sun and P.-Y. Chen, *J. Electrochem. Soc.*, 2016, **163**, D9–D16.
16 V. C. Kieling, *Surf. Coat. Technol.*, 1997, **96**, 135–139.
17 G. P. Pavithra and A. C. Hegde, *Appl. Surf. Sci.*, 2012, **258**, 6884–6890.
18 S. Anand Kumar, S. R. Suseendiran, S. Pavithra, S. Mohan and J. Vijayakumar, *Int. J. Hydrogen Energy*, 2013, **38**, 10208–10214.
19 F. Liu, Y. Deng, X. Han, W. Hu and C. Zhong, *J. Alloys Compd.*, 2016, **654**, 163–170.
20 A. P. Abbott and K. J. McKenzie, *Phys. Chem. Chem. Phys.*, 2006, **8**, 4265–4279.
21 H. P. Nguyen, M. Wu, J. Su, R. J. M. Vullers, P. M. Vereecken and J. Fransaer, *Electrochim. Acta*, 2012, **68**, 9–17.
22 M. Galiński, A. Lewandowski and I. Stępniak, *Electrochim. Acta*, 2006, **51**, 5567–5580.
23 X. Lu and C. Zhao, *Nat. Commun.*, 2015, **6**, 6616.
24 M. W. Louie and A. T. Bell, *J. Am. Chem. Soc.*, 2013, **135**, 12329–12337.
25 X. Li, F. C. Walsh and D. Pletcher, *Phys. Chem. Chem. Phys.*, 2011, **13**, 1162–1167.
26 L.-K. Wu, Y.-X. Zhu, M. Liu, G.-Y. Hou, Y.-P. Tang, H.-Z. Cao, H.-B. Zhang and G.-Q. Zheng, *Int. J. Hydrogen Energy*, 2019, **44**, 5899–5911.
27 U. Y. Qazi, C.-Z. Yuan, N. Ullah, Y.-F. Jiang, M. Imran, A. Zeb, S.-J. Zhao, R. Javaid and A.-W. Xu, *ACS Appl. Mater. Interfaces*, 2017, **9**, 28627–28634.
28 A. P. Abbott, W. Karim and K. S. Ryder, in *Electrodeposition from Ionic Liquids*, ed. F. Endres, A. Abbott and D. MacFarlane, Wiley-VCH, Germany, 2017, p. 412.
29 S. Costovici, A.-C. Manea, T. Visan and L. Anicai, *Electrochim. Acta*, 2016, **207**, 97–111.
30 E. A. Mernissi Cherigui, K. Sentosun, P. Bouckenooge, H. Vanrompay, S. Bals, H. Terryn and J. Ustarroz, *J. Phys. Chem. C*, 2017, **121**, 9337–9347.
31 A. P. Abbott, G. Frisch, J. Hartley, W. O. Karim and K. S. Ryder, *Prog. Nat. Sci.: Mater. Int.*, 2015, **25**, 595–602.
32 C.-D. Gu and J.-P. Tu, *RSC Adv.*, 2011, **1**, 1220–1227.
33 A. P. Abbott, A. Ballantyne, R. C. Harris, J. A. Juma, K. S. Ryder and G. Forrest, *Electrochim. Acta*, 2015, **176**, 718–726.
34 J. M. Hartley, C.-M. Ip, G. C. H. Forrest, K. Singh, S. J. Gurman, K. S. Ryder, A. P. Abbott and G. Frisch, *Inorg. Chem.*, 2014, **53**, 6280–6288.

35 T. R. Griffiths and R. K. Scarrow, *Trans. Faraday Soc.*, 1969, **65**, 3179–3186.
36 R. Li, Q. Dong, J. Xia, C. Luo, L. Sheng, F. Cheng and J. Liang, *Surf. Coat. Technol.*, 2019, **366**, 138–145.
37 D. Yue, Y. Jia, Y. Yao, J. Sun and Y. Jing, *Electrochim. Acta*, 2012, **65**, 30–36.
38 M. Y. Gao, C. Yang, Q. B. Zhang, Y. W. Yu, Y. X. Hua, Y. Li and P. Dong, *Electrochim. Acta*, 2016, **215**, 609–616.
39 C.-W. Su, E.-L. Wang, Y.-B. Zhang and F.-J. He, *J. Alloys Compd.*, 2009, **474**, 190–194.
40 S.-H. Kim, H.-J. Sohn, Y.-C. Joo, Y.-W. Kim, T.-H. Yim, H.-Y. Lee and T. Kang, *Surf. Coat. Technol.*, 2005, **199**, 43–48.
41 T. Yanai, K. Shiraishi, Y. Watanabe, M. Nakano, T. Ohgai, K. Suzuki and H. Fukunaga, *IEEE Trans. Magn.*, 2014, **50**, 1–4.
42 Y. H. You, C. D. Gu, X. L. Wang and J. P. Tu, *Surf. Coat. Technol.*, 2012, **206**, 3632–3638.
43 L. Wang, Y. Gao, Q. Xue, H. Liu and T. Xu, *Appl. Surf. Sci.*, 2005, **242**, 326–332.
44 N. Zech, E. J. Podlaha and D. Landolt, *J. Electrochem. Soc.*, 1999, **146**, 2886–2891.
45 T. Yanai, K. Shiraishi, T. Akiyoshi, K. Azuma, Y. Watanabe, T. Ohgai, T. Morimura, M. Nakano and H. Fukunaga, *AIP Adv.*, 2016, **6**, 055917.
46 K. S. Dijith, R. Aiswarya, M. Praveen, S. Pillai and K. P. Surendran, *Mater. Chem. Front.*, 2018, **2**, 1829–1841.
47 L. Jinlong, L. Tongxiang and W. Chen, *Energy*, 2016, **112**, 67–74.
48 C. A. Melendres and M. Pankuch, *J. Electroanal. Chem.*, 1992, **333**, 103–113.
49 Y. Liu, Z. Fang, L. Kuai and B. Geng, *Nanoscale*, 2014, **6**, 9791–9797.
50 J. Geng, L. Kuai, E. Kan, Y. Sang and B. Geng, *Chem. – Eur. J.*, 2016, **22**, 14480–14483.
51 L. Trotochaud, S. L. Young, J. K. Ranney and S. W. Boettcher, *J. Am. Chem. Soc.*, 2014, **136**, 6744–6753.
52 Y. Qiu, L. Xin and W. Li, *Langmuir*, 2014, **30**, 7893–7901.
53 Y. Liu, N. Han, J. Jiang and L. Ai, *Int. J. Hydrogen Energy*, 2019, **44**, 10627–10636.
54 M. Görlin, P. Chernev, J. de Araújo, T. Reier, S. Dresp, B. Paul, R. Krähnert, H. Dau and P. Strasser, *J. Am. Chem. Soc.*, 2016, **138**, 5603–5614.
55 R. D. L. Smith, M. S. Prévot, R. D. Fagan, S. Trudel and C. P. Berlinguette, *J. Am. Chem. Soc.*, 2013, **135**, 11580–11586.
56 M. S. Burke, M. G. Kast, L. Trotochaud, A. M. Smith and S. W. Boettcher, *J. Am. Chem. Soc.*, 2015, **137**, 3638–3648.
57 K. Fominykh, P. Chernev, I. Zaharieva, J. Sicklinger, G. Stefanic, M. Döblinger, A. Müller, A. Pokharel, S. Böcklein, C. Scheu, T. Bein and D. Fattakhova-Rohlfing, *ACS Nano*, 2015, **9**, 5180–5188.
58 Y. Chen, C. Dong, J. Zhang, C. Zhang and Z. Zhang, *J. Mater. Chem. A*, 2018, **6**, 8430–8440.
59 P. Zhang, L. Li, D. Nordlund, H. Chen, L. Fan, B. Zhang, X. Sheng, Q. Daniel and L. Sun, *Nat. Commun.*, 2018, **9**, 381.
60 M. Tahir, L. Pan, F. Idrees, X. Zhang, L. Wang, J.-J. Zou and Z. L. Wang, *Nano Energy*, 2017, **37**, 136–157.
61 J. Jiang, C. Zhang and L. Ai, *Electrochim. Acta*, 2016, **208**, 17–24.
62 J. Qi, W. Zhang, R. Xiang, K. Liu, H.-Y. Wang, M. Chen, Y. Han and R. Cao, *Adv. Sci.*, 2015, **2**, 1500199.
63 X. W. Yu, M. Zhang, W. J. Yuan and G. Q. Shi, *J. Mater. Chem. A*, 2015, **3**, 6921–6928.
64 F. Song and X. Hu, *Nat. Commun.*, 2014, **5**, 4477.
65 X. Zhang, H. Xu, X. Li, Y. Li, T. Yang and Y. Liang, *ACS Catal.*, 2016, **6**, 580–588.
66 B. Li, S. Chen, J. Tian, M. Gong, H. Xu and L. Song, *Nano Res.*, 2017, **10**, 3629–3637.
67 C. Deng, K.-H. Wu, J. Scott, S. Zhu, R. Amal and D.-W. Wang, *ChemElectroChem*, 2018, **5**, 732–736.
68 S. Ci, S. Mao, Y. Hou, S. Cui, H. Kim, R. Ren, Z. Wen and J. Chen, *J. Mater. Chem. A*, 2015, **3**, 7986–7993.